Available online at www.sciencedirect.com
SCIENCE DIRECT®
Acta Materialia 53 (2005) 1799–1807
Acta MATERIALIA
www.actamat-journals.com

Dynamics of the self-assembly of nanovoids and nanobubbles in solids

Hui-Chia Yu, Wei Lu *

Department of Mechanical Engineering, University of Michigan, 2250 GGBrown, Ann Arbor, MI 48109, USA

Received 15 October 2004; received in revised form 14 December 2004; accepted 16 December 2004
Available online 19 January 2005

Abstract

Experiments show that vacancies in solids may coalesce into voids and self-organize into a superlattice. The voids have diameters around 10 nm and spacing of tens of nanometers. This paper develops a phase-field model to study this behavior, which incorporates the free energy of mixing, interfacial energy and elastic energy. Vacancy diffusion is described by a Cahn–Hilliard type nonlinear diffusion equation, which couples the vacancy distribution field and the stress field. The reduction of the mixing energy drives spinodal decomposition. The reduction of the interfacial energy drives void coarsening. The long-range elastic interaction and elastic anisotropy significantly affect superlattice formation and may essentially limit void coarsening.

Keywords: Self-organization and patterning; Phase-field models; Spinodal decomposition; Nanostructure

1. Introduction

Self-organized periodic array of nanovoids has received considerable attention in recent years for its potential in nanofabrication. The first discovery of the phenomena goes back to Evans [1]. Subjected to continual irradiation of neutrons or heavy particles at elevated temperatures, vacancies emerge in molybdenum and agglomerate into voids. These voids form a three-dimensional body-centered cubic (bcc) lattice structure, replicating the crystal lattice of the host material. The axes of the void superlattice are parallel to those of the host crystal. The ordered voids have diameters around 5–7 nm and lattice spacing around 20–30 nm. Similar phenomena have been experimentally observed in several material systems, including metals such as W [2], Nb [3], Ni [4], alloys such as Mo–Ti [5], Ni–Al [6], Cu–Ni [7] and compounds such as CaF_2 [8], NaCl [9]. Analogous bubble lattices, such as in helium [10], are reported under gaseous ion irradiation at lower temperature (from room temperature to 0.2 melting temperature). Self-assembled bubbles are generally smaller than voids. The diameters are about 2–3 nm and the superlattice spacing are around 5–7 nm. Another type of self-ordered defect clusters has also been reported. Jager and Trinkaus [11] have shown that after relatively low dose of irradiation on copper and nickel, the vacancy regions form well aligned labyrinth-like defect walls. These walls are parallel to the close-packed directions of the host crystals. Despite the difference in the appearance, a similar underlying mechanism may be invoked to explain the self-organization behavior.

Experimental observations have revealed some general features [12,13]. Tiny voids appear randomly in the early stage of irradiation. These voids grow and start ordering under continual irradiation (usually a couple to tens of hours [4]) at about 0.3–0.4 melting temperature of the specimens. Then the ordering of voids expands

* Corresponding author. Tel.: +1 734 647 7858; fax: +1 734 647 3170.
E-mail address: weilu@umich.edu (W. Lu).

1359-6454/$30.00
doi:10.1016/j.actamat.2004.12.029

from many early formed small ''seed'' regions to other regions. There exists a threshold value of irradiation dose depending on materials, and the lattice perfection increases with the dose. However, the void ordering is insensitive to the dose rate. In contrast to the widely seen bcc void superlattice, a well-developed face-centered cubic (fcc) lattice has only been experimentally observed in nickel, and requires a much higher dosed irradiation.

Different models have been proposed to explain the formation and property of the void lattice. They fall into four main categories. The first class of models is based on the quasi-elastic analysis. Willis and Bullough [14] calculated the elastic energy of an infinitely large elastic solid containing two voids or bubbles. Their results showed that in an isotropic medium two voids or bubbles will always attract each other until they coalesce. In contrast, Willis [15] showed that the energy of two equal-sized voids or bubbles in an anisotropic medium (molybdenum) could reach a minimum at a particular distance. The ratio between the separation distance and the void radius is 3.22. Stoneham [16] calculated the elastic energy of an entire void superlattice in an anisotropic medium with a prior assumption of the type and the axial directions of the lattice. His results suggested that the elastic energy minimized at the distance–radius ratio of 3.1 for bcc crystals and 2.2 for fcc crystals. These analyses highlight the significant role of elastic anisotropy in the void/bubble lattice formation. However, the prior assumption of void shape and lattice type precludes many possible patterns. The models can determine the ratio between void radius and superlattice spacing, but the absolute void size and lattice dimension remain unknown. In particular, the models cannot describe the dynamic ordering process.

The second class of models is based on the concept of crystallographic anisotropic diffusion of self-interstitial atoms (SIA) in host materials [17]. SIAs and vacancies are concurrently generated during particle irradiation. A configuration of crowdion, consisting of SIAs, is created in the neighborhood of a void. SIAs are supposed to have orientational preference of migration due to the crystal structures, and the crowdions are aligned along the close-packed directions. The crowdions extend from the void surface, forming crowdion supply cylinders (CSC) that provide atoms to shrink the voids. The radius of each cylinder is equal to the radius of the void that the crowdion belongs to. When the separation of two voids is sufficiently small along the closed-packed directions, their CSCs overlap. As a result, the interstitial flux toward both voids decreases. In other words, the net vacancy flux toward the two voids increases, enhancing the void growth rate. Eventually, only aligned voids survive throughout the irradiation process, and the distance between voids is the length of CSC. This class of models provides an explanation of isomorphic behavior between void/bubble superlattice and host crystal lattice. Nevertheless, as argued by Krishan [18] and Dubinko et al. [13], the length of CSC decreases exponentially with temperature. This is not consistent with experimental observations. In fact, long-range ordering has been reported at relatively high temperature. Another concern is the lack of direct evidence to support the existence of CSC and the anisotropic migration behavior of SIA. These models disregard the possible relation between point defect diffusion and material elasticity. This might not be satisfactory when considering vacancy migration in an elastic medium.

The third class of models relies on the interaction between dislocations and cavities (voids/bubbles) [13,19,20]. Interstitial loops (dislocations) are punched out (or absorbed) due to the pressure exerted by the entrapped gas inside bubbles (or the surface tension of void surfaces). These dislocations have orientational preference along the crystal close-packed directions. In the models, different mechanisms are assumed for the formation of bubble and void superlattices. The bubble lattice is formed by the balance between repulsive (between dislocations and bubbles) and attractive (between bubble and bubble) forces. Void lattice is formed by the anisotropic diffusion of interstitial loops. The interstitial loops are attracted toward voids along the crystal close-packed directions, forming loop supply cylinders (LSC). When LSCs of two voids overlap, the supply of interstitial loops toward each void drops drastically. On the other hand, those disordered voids keep absorbing interstitial loops and shrink. Eventually only ordered voids survive. In these models, void lattice formation is considered as a natural selection of survival voids, which is essentially similar to anisotropic diffusion models. The models require pre-existing bubbles or voids. The dynamics of bubble/void formation and coalescent process are not considered.

The fourth class of models is based on the microstructure-induced instability. Krishan [18] suggested that point and extended defects are produced during particle irradiation. Point defects, such as vacancies and interstitial atoms, are assumed to be mobile. Extended defects are considered immobile, which include vacancy and interstitial clusters, such as voids or dislocation loops. Extended defects are distributed randomly and serve as sinks for point defects. The combination of the defect generation rate, recombination effect and defect migration leads to a set of rate equations describing the dynamics of defect concentrations. Periodic concentration profiles of vacancies are obtained by solving the eigenvalue problems. Another series of instability analyses were performed by Walgraef and co-workers [21,22]. More complicated defect species and orientational preference of mobile defects are considered. The amplitude of vacancy clusters is shown to distribute periodically,

such as bcc and fcc void lattices. The results give perspective relations between defect distribution and environment conditions. Based solely on orientational preference of defect mobility, the models have neglected the possible influence of elasticity.

We propose to develop a model that considers both elasticity and the dynamic diffusion process. Experiments and analytical studies highlight two observations. One is phase separation. A pure metal phase separates into two phases under irradiation: a vacancy-rich phase and a phase rich in the interstitial atom. In other words, the irradiation provides enough activation energy to induce a type of spinodal decomposition. The other one is anisotropic diffusion, which causes vacancies to accumulate at certain ordered positions. We will show that the diffusion anisotropy has close relation to the elastic anisotropy. We adopt a phase field approach in our model. The application of a diffuse interface allows voids or bubbles to emerge or dissolve naturally, and the system can form whatever lattice it favors. Voids are treated as high vacancy concentration regions. Dynamic processes, such as void coalescence, are captured by updating the concentration profile over time. Elastic effects due to the existence of vacancies are calculated by the microelasticity theory [24]. We incorporate the free energy of mixing, interfacial energy and elastic strain energy into the driving force for vacancy diffusion. The simulations suggest that the elastic anisotropy can induce orientational preference in vacancy diffusion, even if the diffusivity is isotropic. It is found that vacancies migrate faster along the elastic compliant directions. This causes the self-assembled voids to replicate the host crystal symmetry. Our work shows that void self-assembly dynamics can be studied via a spinodal decomposition mechanism.

2. Phase-field approach

Imada [23] was among the first to realize that spinodal decomposition might be a reason for void/bubble lattice formation. He calculated the relation between the chemical free energy and the vacancy concentration instability, suggesting that the lost of stability may lead to periodic vacancy structures. Here we also assume spinodal decomposition as one possible mechanism during the void/bubble superlattice formation. In the formulation, we use void lattice as the example. Bubble lattice can be analyzed similarly. Generally speaking, the irradiation generates a significant amount of vacancies in a crystal. The corresponding mixing energy is large if the vacancies distribute uniformly in the crystal. This drives phase separation. We focus on the annealing process after the irradiation has stopped, and demonstrate that annealing a crystal with high vacancy content produces various void lattices. The detail of the model is discussed below.

Vacancies are produced randomly in a crystal during particle irradiation. A spatially continuous and time-dependent function, $c(\mathbf{x}, t)$, describes the vacancy distribution. Here $c(\mathbf{x}, t)$ represents the fraction of atomic sites occupied by vacancies at position $\mathbf{x}$, where $\mathbf{x} = (x_1, x_2, x_3)$ are the spatial coordinates. The total free energy of the system is

$$G = \int_V [g(c) + \kappa(\nabla c)^2 + g_e]\, \mathrm{d}V, \tag{1}$$

where $g(c)$ is the free energy of mixing, κ is the gradient coefficient, g_e the elastic energy per unit volume, and V is the total volume. The first term represents the mixing energy of vacancies and crystal atoms. To describe phase separation, we may prescribe $g(c)$ as any functional with double wells in terms of the concentration, $c(\mathbf{x}, t)$. Here, we assume a regular solution [24,25], so that

$$g(c) = g_v c + g_a(1-c) + Nk_B T[c\ln c + (1-c)\ln(1-c)] + N\Omega c(1-c), \tag{2}$$

where g_v is the chemical energy of vacancy per unit volume and g_a the chemical energy of crystal atom per unit volume. N is the number of atomic sites per unit volume, k_B is the Boltzmann's constant, and T is the absolute temperature. The parameter Ω determines the shape of $g(c)$. When $\Omega > 2k_B T$, the function has double wells and drives phase separation. The term $\kappa(\nabla c)^2$ represents the interfacial energy, where κ is a material constant. The first two terms are typical in the Cahn–Hilliard equation. The g_e term represents the elastic energy.

Assume that a stress-free strain, $\varepsilon_0\delta_{ij}$, emerges when an atomic site is occupied by a vacancy, where δ_{ij} is the Kronecker delta function. A void differs from a solid precipitate in that it cannot sustain load or store any elastic energy. It is known that atoms at a solid surface have a different lattice parameter from those interior atoms due to the difference in bounding environment. This causes a misfit between the atoms on the void surface and the interior atoms in the solid. We assume that the misfit strain takes the form of $\varepsilon^0_{ij}(\mathbf{x}) = 2\varepsilon_0\delta_{ij}(1-c(\mathbf{x}))c(\mathbf{x})$, so that the strongest misfit appears at the void/solid interface, and vanishes in solid or void. A negative ε_0 generates a contracting force toward the center of a void. The contracting force is conceptually equivalent to surface stress [26], which has been shown to cause surface reconstruction and monolayer self-assembly. A positive ε_0 generates a pressure that is equivalent to the excess pressure acting on a bubble surface by entrapped gas. Different forms of stress-free strains may be used. As long as they capture the major feature that the misfit exists at the interface, the specific function form is insignificant in the limit of vanishing interface thickness. Following common practice, we interpolate the elastic constants of a vacancy–solid com-

posite by $\lambda_{ijlm}(\mathbf{x}) = (1 - c(\mathbf{x}))\lambda^0_{ijlm}$, where λ^0_{ijlm} is the elastic stiffness of solid. The elastic field can be obtained by the supposition of a uniform field and an inhomogeneous perturbation field. The total strain field, $\varepsilon_{ij}(\mathbf{x})$, is expressed by

$$\varepsilon_{ij}(\mathbf{x}) = \bar{\varepsilon}_{ij} + \tilde{\varepsilon}_{ij}(\mathbf{x}), \tag{3}$$

where $\bar{\varepsilon}_{ij}$ is the uniform strain and $\tilde{\varepsilon}_{ij}(\mathbf{x})$ is the inhomogeneous strain. The uniform strain is the macroscopic strain of the vacancy–solid composite relative to a vacancy-free solid, and is expressed by $\bar{\varepsilon}_{ij} = \varepsilon^{\text{app}}_{ij} + \varepsilon_0\delta_{ij}\bar{c}_1$, where $\varepsilon^{\text{app}}_{ij}$ is the macroscopic strain due to applied stress, $\varepsilon_0\delta_{ij}\bar{c}_1$ is the average misfit strain over the volume, and $\bar{c}_1 = (\int_V 2(1 - c(\mathbf{x}))c(\mathbf{x})\,\mathrm{d}V)/V$. The strain $\varepsilon^{\text{app}}_{ij}$ relates to the applied stress σ^{app}_{lm} by $\varepsilon^{\text{app}}_{ij} = (\bar{\lambda}_{ijlm})^{-1}\sigma^{\text{app}}_{lm}$, where $\bar{\lambda}_{ijlm} = \lambda^0_{ijlm}(1 - \bar{c})$, and $\bar{c} = (\int_V c(\mathbf{x})\,\mathrm{d}V)/V$ is the average concentration. The inhomogeneous strain, $\tilde{\varepsilon}_{ij}(\mathbf{x})$, relates to the perturbation displacement, $u_i(\mathbf{x})$, by

$$\tilde{\varepsilon}_{ij}(\mathbf{x}) = \frac{1}{2}\left(\frac{\partial u_i(\mathbf{x})}{\partial x_j} + \frac{\partial u_j(\mathbf{x})}{\partial x_i}\right). \tag{4}$$

The total stress field, $\sigma_{ij}(\mathbf{x})$, can be computed by $\lambda_{ijlm}(\mathbf{x})(\varepsilon_{lm}(\mathbf{x}) - \varepsilon^0_{lm}(\mathbf{x}))$, namely

$$\sigma_{ij}(\mathbf{x}) = \lambda^0_{ijlm}(1 - c(\mathbf{x}))(\varepsilon_{lm}(\mathbf{x}) - \varepsilon^0_{lm}(\mathbf{x})). \tag{5}$$

The system can vary in two ways: elastic deformation and diffusion [25,27]. The energy variation of Eq. (1) to the elastic deformation gives the classic equilibrium equation, $\partial\sigma_{ij}/\partial x_j = 0$. Substitute Eqs. (3)–(5) into this equation, we obtain

$$\lambda^0_{ijlm}\left[\frac{\partial^2}{\partial x_j\partial x_m} - \frac{\partial}{\partial x_j}\left(c(\mathbf{x})\frac{\partial}{\partial x_m}\right)\right]u_l(\mathbf{x}) = \bar{\sigma}_{ij}\frac{\partial c(\mathbf{x})}{\partial x_j} + \sigma^0_{ij}\frac{\partial c_2(\mathbf{x})}{\partial x_j}, \tag{6}$$

where $\bar{\sigma}_{ij} = \lambda^0_{ijlm}\bar{\varepsilon}_{lm}$, $\sigma^0_{ij} = \lambda^0_{ijlm}\delta_{lm}\varepsilon_0$, and $c_2(\mathbf{x}) = 2c(x)(1 - c(\mathbf{x}))^2$. Taking Fourier transform of Eq. (6), we have

$$\hat{u}_l(\mathbf{k}) = -\mathrm{i}k_jG_{il}(\mathbf{k})\left[\bar{\sigma}_{ij}\hat{c}(\mathbf{k}) + \sigma^0_{ij}\hat{c}_2(\mathbf{k}) + \lambda^0_{ijlm}\left(c(\mathbf{x})\frac{\partial u_l(\mathbf{x})}{\partial x_m}\right)_{\mathbf{k}}\right], \tag{7}$$

where the hat denotes Fourier Transform, $\mathbf{k}$ is the wave vector in Fourier space, and $G_{il}(\mathbf{k}) = (\lambda^0_{ijlm}k_jk_m)^{-1}$ is the Green's tensor. We solve Eq. (7) by numerical iteration [28]. The displacement field at the nth iteration is given by

$$\hat{u}^{(n)}_l(\mathbf{k}) = -\mathrm{i}k_jG_{il}(\mathbf{k})\left[\bar{\sigma}_{ij}\hat{c}(\mathbf{k}) + \sigma^0_{ij}\hat{c}_2(\mathbf{k}) + \lambda^0_{ijlm}\left(c(\mathbf{x})\frac{\partial u^{(n-1)}_l(\mathbf{x})}{\partial x_m}\right)_{\mathbf{k}}\right]. \tag{8}$$

The initial value in the iteration is taken to be $\hat{u}^{(0)}_l(\mathbf{k}) = -\mathrm{i}k_jG_{il}(\mathbf{k})[\bar{\sigma}_{ij}\hat{c}(\mathbf{k}) + \sigma^0_{ij}\hat{c}_2(\mathbf{k})]$. The inhomogeneous displacement in real space, $u^{(n)}_l$, is obtained by the inverse Fourier transform of $\hat{u}^{(n)}_l$. The elastic energy density is given by $g_{\text{e}} = \lambda_{ijlm}(\varepsilon_{ij} - \varepsilon^0_{ij})(\varepsilon_{lm} - \varepsilon^0_{lm})/2$.

Now consider the vacancy diffusion. A driving force, P_i, is defined by the amount of free energy reduction when a vacancy moves by a unit distance. Following a similar approach to that in [25], the energy variation of Eq. (1) to vacancy diffusion gives

$$P_i = -\frac{1}{N}\nabla\left(\frac{\delta g}{\delta c} - 2\kappa\nabla^2 c + \frac{\delta g_{\text{e}}}{\delta c}\right). \tag{9}$$

The vacancy flux, J_i, is assumed proportional to the driving force, giving

$$J_i = MP_i, \tag{10}$$

where M is mobility. Combining Eqs. (9) and (10) and the conservation equation $N\partial c/\partial t + \nabla\cdot\mathbf{J} = 0$, we obtain the diffusion equation

$$\frac{\partial c}{\partial t} = \frac{1}{N^2}\nabla\cdot M\nabla\left(\frac{\delta g}{\delta c} - 2\kappa\nabla^2 c + \frac{\delta g_{\text{e}}}{\delta c}\right). \tag{11}$$

The first two terms in the bracket in Eq. (11) is standard in the Cahn–Hilliard equation [29]. The third term reflects the elastic effect. Generally speaking, mobility depends on the local structure and thus the local concentration. Atoms diffuse much faster at the void/solid interface than in the solid. To emphasize interface diffusion, we adopt a concentration-dependent mobility [23,28]. It takes the form of $M(c) = c(1 - c)M$, where M is a constant. Thus the mobility reaches maximum at the void/solid interface and vanishes in pure solid or void. Eq. (11) then becomes

$$\frac{\partial c}{\partial t} = \frac{M}{N^2}\nabla\cdot c(1 - c)\nabla\left(\frac{\delta g}{\delta c} - 2\kappa\nabla^2 c + \frac{\delta g_{\text{e}}}{\delta c}\right). \tag{12}$$

Define the length scale by $b = \sqrt{4\kappa/3Nk_{\text{B}}T}$ and the time-scale by $\tau = \kappa/M(k_{\text{B}}T)^2$. Normalize the coordinates by b and the time by τ, we obtain a dimensionless diffusion equation,

$$\frac{\partial c}{\partial t^*} = \frac{3}{4}\nabla\cdot c(1 - c)\nabla\left(\frac{\delta g^*}{\delta c} - 1.5\nabla^2 c + \frac{\delta g^*_{\text{e}}}{\delta c}\right), \tag{13}$$

where $x^* = x/b$, $t^* = t/\tau$, $g^* = g/Nk_{\text{B}}T$ and $g^*_{\text{e}} = g_{\text{e}}/Nk_{\text{B}}T$. Applying Fourier transform, the diffusion equation in Fourier space is given by

$$\frac{\partial\hat{c}}{\partial t^*} = \frac{3}{4}\mathrm{i}\mathbf{k}\cdot\{c(1 - c)[\mathrm{i}\mathbf{k}(\hat{\mu} + 1.5k^2\hat{c} + \hat{\mu}_{\text{e}})]_{\mathbf{r}}\}_{\mathbf{k}}, \tag{14}$$

where the subscript '**r**' denotes inverse Fourier transform,

$$\mu = \delta g^*/\delta c = \ln(c/(1 - c)) + (1 - 2c)\Omega/k_{\text{B}}T \tag{15}$$

and

$$\mu_e = \delta g_e^*/\delta c = -\frac{1}{2}\frac{\lambda^0_{ijkl}}{Nk_BT}(\bar{\varepsilon}_{ij}+\tilde{\varepsilon}_{ij}(\mathbf{x}))(\bar{\varepsilon}_{kl}+\tilde{\varepsilon}_{kl}(\mathbf{x})) + \frac{\lambda^0_{ijkl}}{Nk_BT} \times (\bar{\varepsilon}_{ij}+\tilde{\varepsilon}_{ij}(\mathbf{x}))\delta_{kl}\varepsilon_0(1-c(\mathbf{x}))(3c(\mathbf{x})-1) + \frac{1}{2}\frac{\lambda^0_{ijkl}}{Nk_BT}\delta_{ij}\delta_{kl}\varepsilon_0^2 c(\mathbf{x})(2-5c(\mathbf{x}))(1-c(\mathbf{x}))^2. \quad (16)$$

To track the evolution of Eq. (14), we adopt a time marching scheme that has proved computational stability [30],

$$(1+\alpha A k^4 \Delta t^*)\hat{c}^{(m)} = (1+\alpha A k^4 \Delta t^*)\hat{c}^{(m-1)} + \frac{3}{4}\Delta t^* i\mathbf{k}\cdot\{c^{(m-1)}(1-c^{(m-1)}) \times [\mathbf{i}\mathbf{k}(\hat{\mu}^{(m-1)} + \alpha k^2 \hat{c}^{(m-1)} + \hat{\mu}_e^{(m-1)})]_{\mathbf{r}}\}_{\mathbf{k}}, \quad (17)$$

where m denotes the mth time step, $\alpha = 1.5$ is the dimensionless gradient coefficient, and A is a coefficient stabilizing time marching scheme. We choose $A = \frac{1}{2}[\max((1-c)c) + \min((1-c)c)]$ in our work.

3. Numerical results

Several parameters are required to simulate the dynamic evolution of vacancies. We use the material properties of molybdenum and nickel in the computation. The gradient coefficient, κ, dependents on the lattice structure and the inter-atomic energy [29]. Its value is usually estimated by $\theta N k_B T r_0^2$, where θ is a coefficient dependent on material, and r_0 is the nearest neighbor distance. The magnitude of κ is in the order of 10^{-10} J m^{-1}. In the simulation of molybdenum, we take $\kappa \sim 2\times10^{-10}$ J m^{-1}, a lattice constant of 3.2 Å, and an irradiation/annealing temperature of 1100 K. Boltzmann's constant is 1.38×10^{-23} J K^{-1}. Combining these values, the length scale b for molybdenum is $b_{Mo} \sim 0.53$ nm. Similarly, the length scale for nickel, $b_{Ni} \sim 1.3$ nm, is obtained by setting $\kappa \sim 1.2\times10^{-9}$ J m^{-1}, a lattice constant of 3.54 Å, and an irradiation/annealing temperature of 800 K. The elastic constants for molybdenum are taken to be $C_{11} = 347.6$, $C_{12} = 121.8$ and $C_{44} = 81.5$, all in the unit of Nk_BT. The elastic constants of nickel are taken to be $C_{11} = 160.6$, $C_{12} = 99.7$ and $C_{44} = 81.3$, all in the unit of Nk_BT. A single vacancy is typically considered to have a volume of 40% atomic volume of the surrounding atom. For constrained elastic misfit (in situ misfit), ε_0 is usually taken between $e/6$ and $e/3$, where e is the volume shrinkage strain. In our simulation, we take ε_0 to be -0.1.

The elastic field affects diffusion through a chemical potential, $\mu_e = \delta g_e^*/\delta c$. To better understand this effect, we calculate the elastic field of a two-dimensional square domain containing a circular high vacancy concentration region at the center. The square has a size of 128×128 grid points and a concentration of 0.1, while the circular region has a radius of eight grid points and a concentration of 0.95. Two situations, molybdenum and nickel, are calculated. Molybdenum has a bcc structure and is compliant in the ⟨1,1⟩ directions, while nickel has fcc structure and is compliant in the ⟨1,0⟩ directions. The calculations show that the iteration algorithm of Eq. (8) converges quickly, usually within four to five iterations. The results are confirmed by finite element computations. Fig. 1 shows the distribution of μ_e. Strong anisotropy can be observed. For molybdenum, the magnitude of μ_e is higher in the ⟨1,0⟩ directions and lower in the ⟨1,1⟩ directions, as shown in Fig. 1(a). A vacancy would prefer to stay in a lower μ_e region, i.e., along the ⟨1,1⟩ directions. A void is an agglomeration of vacancies. When two voids are close to each other, they would align along the ⟨1,1⟩ directions for lower chemical potential. However, for nickel μ_e is higher in the ⟨1,1⟩ directions and lower in the ⟨1,0⟩ directions, as shown in Fig. 1(b). Consequently, the voids tend to align along the ⟨1,0⟩ directions. For both cases, the lower μ_e directions coincide with the elastic compliant directions, and also the close-packed directions of the crystals.

A series of simulations are performed for dynamic void lattice formation and evolution by Eq. (17). The computation cell is 128×128 grid points. The boundary

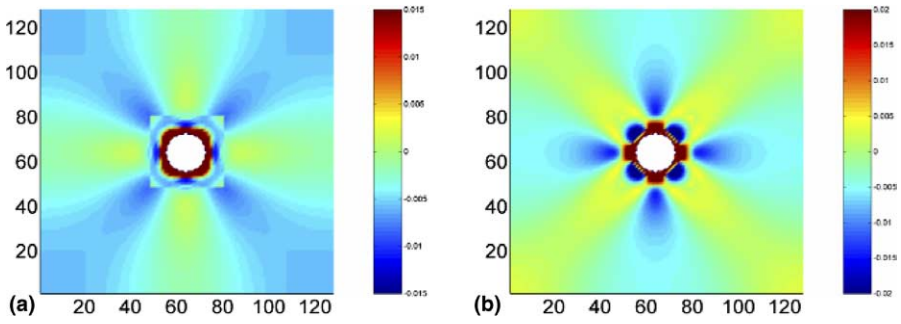

Fig. 1. The elastic chemical potential distribution of: (a) molybdenum and (b) nickel.

conditions are periodic. Our simulation of two voids in an isotropic medium confirmed the theoretical prediction based on energetic analysis [14]: they attract each other and eventually coalesce. Now consider the void lattice formation in an anisotropic solid. A large amount of vacancies are generated during the irradiation process. Experimental observations suggest that the average vacancy concentration in a well developed void lattice is about 0.32. We use random initial condition in the simulation, which has an average of 0.32 and perturbation amplitude of 0.001. At present, we assume there is no external loading. In the simulation for molybdenum, we use $\Omega/k_BT = 2.9$ and a time step of $\Delta t^* = 0.33$. Fig. 2 shows the simulation results. It can be observed that ordered voids first emerge in several small regions and then spread throughout entice computation cell. Disordered voids are also seen during the evolution. However, they shrink over time and eventually disappear. Voids self-align along the $\langle 1,1 \rangle$ directions, showing almost uniform size and spacing. We have calculated longer evolution time beyond Fig. 2(h). The pattern did not change much, suggesting that further evolution is very slow. The diameter of the voids is about 12 grid spaces, or 6–7 nm. The superlattice spacing is about 32 grid spaces, or 17–

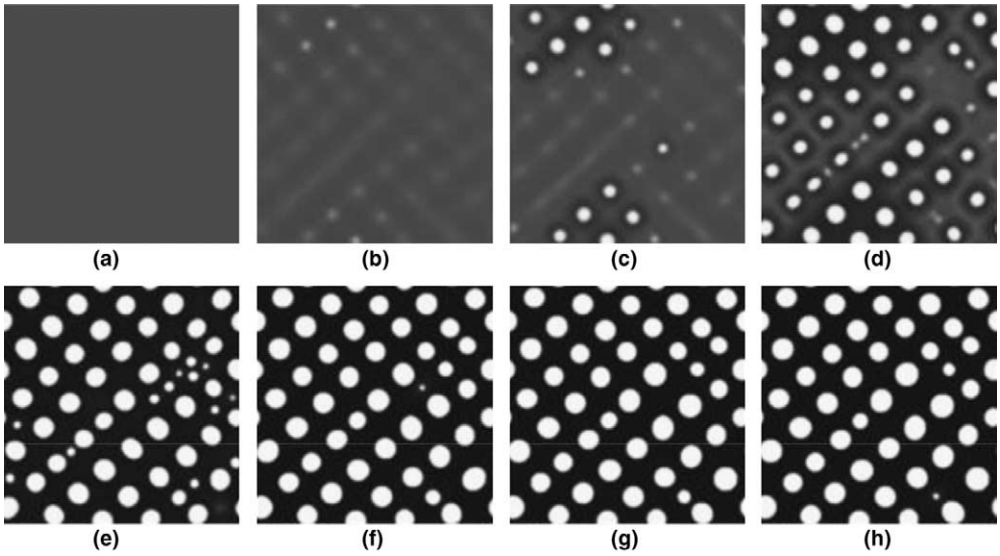

Fig. 2. The formation and pattern evolution of voids in molybdenum. $\Omega/k_BT = 2.9$, $\Delta t^* = 0.33$. (a) $t^* = 0$, (b) $t^* = 799.92$, (c) $t^* = 823.68$, (d) $t^* = 850.08$, (e) $t^* = 892.32$, (f) $t^* = 1016.40$, (g) $t^* = 1201.20$ and (h) $t^* = 1440.12$.

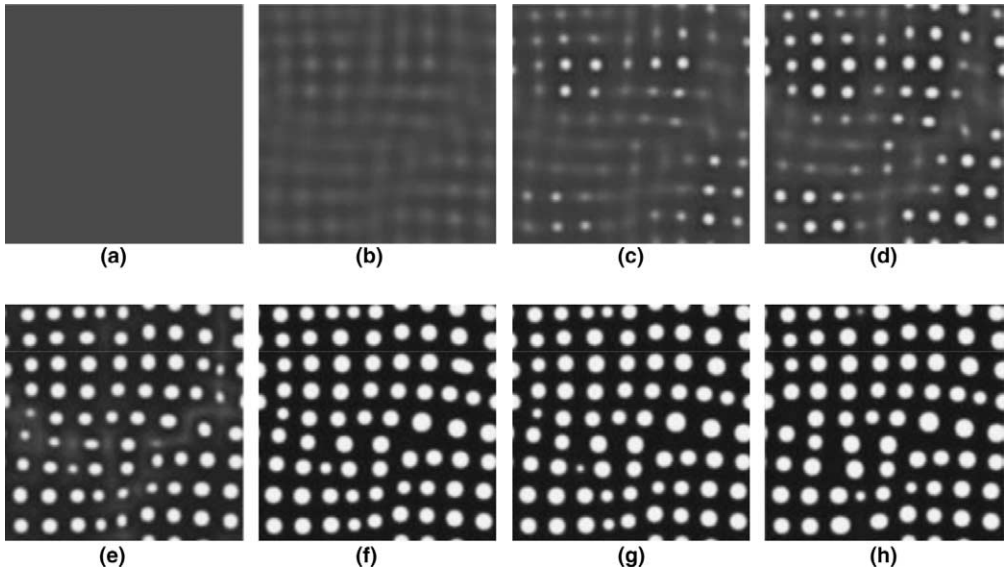

Fig. 3. The formation and pattern evolution of voids in nickel. $\Omega/k_BT = 2.8$, $\Delta t^* = 0.533$. (a) $t^* = 0$, (b) $t^* = 386.43$, (c) $t^* = 406.95$, (d) $t^* = 418.67$, (e) $t^* = 437.86$, (f) $t^* = 613.22$, (g) $t^* = 869.59$ and (h) $t^* = 1124.36$.

20 nm. Note that the coordinates are normalized by b_{Mo}. The physical length is grid space multiplied by b_{Mo}.

Similar simulations were performed for nickel. The same initial conditions were used. Other parameters are $\Omega/k_BT = 2.8$ and $\Delta t^* = 0.533$. The results are shown in Fig. 3. Similarly, ordered voids loom out in several small regions and the order expands. Disordered voids gradually dissolve. The diameters of the voids is about 11 grid spaces, or 14–15 nm. The superlattice spacing is about 35 grid spaces, or 45–50 nm. The morphology and length scale of our simulations are consistent with experiments. We have also simulated void lattice for copper, where labyrinth-like stripes orientating along the $\langle 1,0\rangle$ directions are obtained. We find that a host material with strong elastic anisotropy prefers the formation of defect walls, instead of spherical voids.

Now consider the bubble lattice formation. In the simulation for molybdenum, we assume that an implanted gas atom causes an in situ lattice misfit of $\varepsilon_0 = 0.05$ when it occupies a lattice site. This causes a pressure on bubble surfaces. The irradiation temperature is taken to be 300 K. At this temperature, the elastic constants of molybdenum are taken to be $C_{11} = 1069.6$, $C_{12} = 374.9$ and $C_{44} = 250.7$, all in unit of Nk_BT. We set the gradient coefficient κ to be 0.2×10^{-10} J m^{-1}, which gives the length scale of $b_{Mo} \sim 0.3$ nm . Same initial and boundary conditions are applied. Fig. 4 shows the simulation results. The evolution process and morphology are very similar to those in void lattice, except that the bubbles have smaller sizes.

Simulations are also extended to investigate the influence of external loadings. A shear loading of $\tau_{xy} = 2Nk_BT$ is applied to the computation cell. This causes the formation of a slit-like void structure orientating in the [1,1] direction, as shown in Fig. 5. However, when the load is low, the voids may still have a shape close to a sphere. This is observed in Fig. 6, which shows the results for nickel with an applied load of $\tau_{xy} = 1Nk_BT$. Our simulation with other loading conditions suggest that a small load will shift the orientation of self-assembled voids, while a large load will also significantly influence the void shape. The self-assembled features may change from spheres, to ellipsoids, and to slits as the load increases. When a uniaxial load is

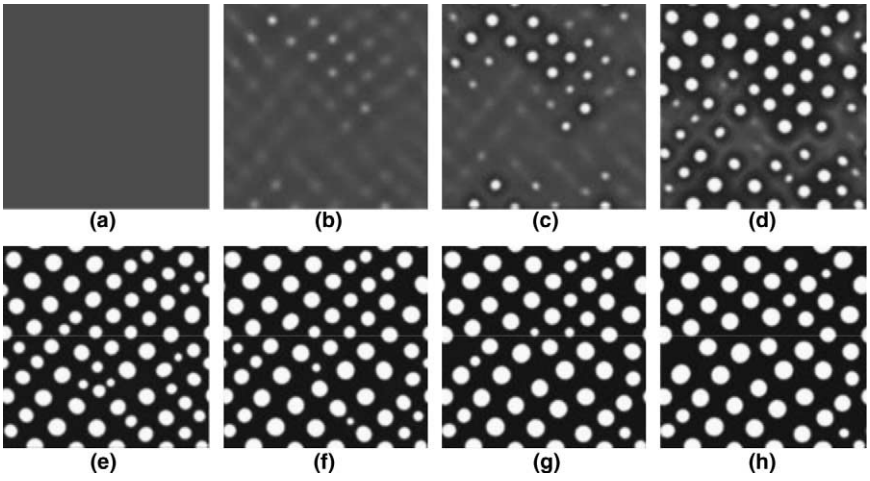

Fig. 4. The formation and pattern evolution of bubbles in molybdenum. $\Omega/k_BT = 2.9$, $\Delta t^* = 0.33$. (a) $t^* = 0$, (b) $t^* = 339.24$, (c) $t^* = 351.12$, (d) $t^* = 369.60$, (e) $t^* = 404.58$, (f) $t^* = 582.78$, (g) $t^* = 803.22$ and (h) $t^* = 978.78$.

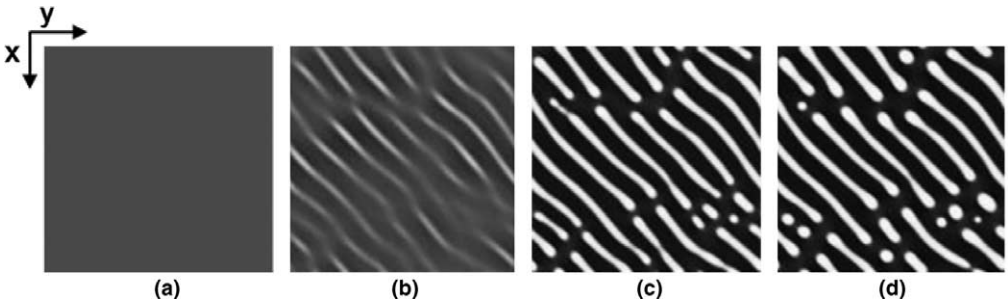

Fig. 5. The formation and pattern evolution of voids in molybdenum under the loading of $\tau_{xy} = 2Nk_BT$. (a) $t^* = 0$, (b) $t^* = 192.72$, (c) $t^* = 224.40$ and (d) $t^* = 299.64$.

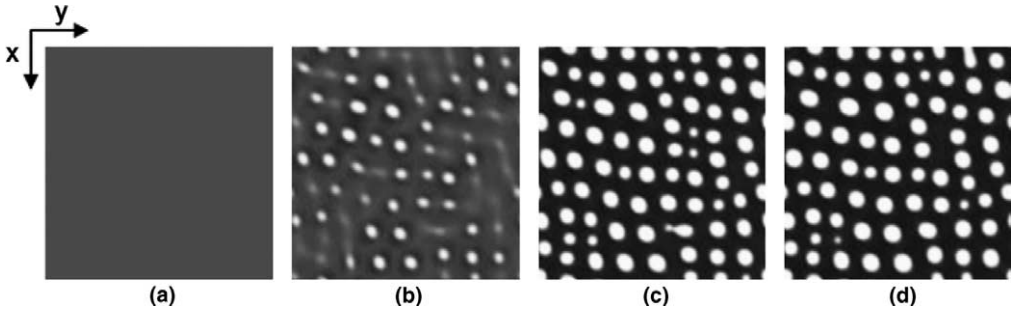

Fig. 6. The formation and pattern evolution of voids in nickel under the loading of $\tau_{xy} = Nk_BT$. (a) $t^* = 0$, (b) $t^* = 289.08$, (c) $t^* = 324.72$, (d) $t^* = 398.31$.

applied along the symmetric directions, such as $\langle 1,0 \rangle$ or $\langle 1,1 \rangle$, a void has a longer dimension in perpendicular to the load vector. However, a general loading condition is complicated by the elastic anisotropy, and numerical simulation is needed.

4. Discussion

In this work, we show that annealing a crystal with high vacancy content can lead to a self-assembled void lattice. In experiments, a crystal is put under irradiation at elevated temperature for a long time for void lattice to form. The high environmental temperature and irradiation effect significantly increase the mobility of vacancies, allowing them to diffuse over a long distance during the experimental period. Consequently, an annealing process may exist and account for the observed phenomena. This paper treats it by an approach of spinodal decomposition. Accompanying the phase separation, vacancies diffuse and agglomerate into voids. The void formation induces elastic interaction, causing directional preference of vacancies. Consequently, phase separation and anisotropic diffusion are two significant aspects in self-assembled void lattices. It is similar for the case of implanted gas agglomerating into bubbles. From the energetic point of view, phase separation reduces the mixing energy, but increases the elastic energy. Our simulations show that when voids/bubbles self-organize along certain directions, the elastic energy increase is minimized. Those early forming voids serve as anchors. Subsequent voids arrange themselves along specific directions of the anchoring voids, leading to the observed order spreading phenomena. For the same reason, unaligned voids shrink and disappear.

Our model suggests that self-ordering may occur only when voids/bubbles are close enough to within each other's elastic influence range. Thus a certain void/bubble density is required to form a superlattice. This might explain the existence of a threshold of irradiation dose for void/bubble lattice formation. Temperature has several effects. In addition to increasing mobility, an elevated temperature also reduces the elastic stiffness of host crystals and thus influences the void size. External loadings are influential to the patterns of void/bubble superlattices, according to the simulations. Together with the elastic misfit, the external loadings contribute to the elastic chemical potential. This implies that the morphology and size of nanoscale voids/bubbles can be tuned by altering the loading conditions.

We have demonstrated anisotropic diffusion of point defects due to material anisotropy from a purely energetic point of view. Kinetically, the mobility may also depend on material structure and be anisotropic. This effect will be pursued in further study. Our model can be expanded to incorporate structural order parameters and interface energy anisotropy. This may help to explain the appearance of some cubical [4] or facet [8] voids.

In summary, we have developed a phase field model to simulate the void/bubble self-organizing behavior. In particular, we emphasize the interface misfit. The results are consistent with experimental observations, and suggest that void lattices, bubble lattices and labyrinth defect walls may be explained in the same framework. Complementing other proposed mechanisms, we show that phase separation, material anisotropy and annealing can also produce ordered patterns of voids/bubbles.

Acknowledgment

The authors acknowledge financial support from National Science Foundation Career Award No. DMI-0348375.

References

[1] Evans JH. Nature 1971;229:403.
[2] Moteff J, Sikka VK, Jang H. In: Consultant symposium on the physics of irradiation produced voids. A.E.R.E. Harwell; 1975. p. 181.
[3] Kulcinski GL, Brimhall JL, Kissinger HE. In: Proceedings of the international conference on radiation-induced voids in metals. Springfield (VA): National Technological Information Service; 1972. p. 465.

[4] Kulcinski GL, Brimhall JL. Effects of radiation on substructure and mechanical properties of metals and alloys. Philadelphia: American Society for Testing and Materials; 1973.
[5] Wiffen FW. In: Proceedings of the International Conference on Radiation-Induced voids in Metals. Springfield (VA): National Technological Information Service; 1972.
[6] Chen LJ, Ardell AJ. J Nucl Mater 1978;75:177.
[7] Zinkle SJ, Singh BN. Nucl Mater 2000;283&287:306.
[8] Johnson E, Chadderton LT. Radiat Eff 1983;79:183.
[9] Vainshtein DI, Altena C, den Hartog HW. Mater Sci Forum 1997;239&241:607.
[10] Johnson PB, Mazey DJ. J Nucl Mater 1995;218:273.
[11] Jager W, Trinkaus H. J Nucl Mater 1993;205:394.
[12] Cahn RW. Nature 1979;281:338.
[13] Dubinko VI, Tur AV, Turkin AA, Yanovski VV. J Nucl Mater 1989;161:57.
[14] Willis JR, Bullogh R. J Nucl Mater 1969;32:76.
[15] Willis JR. J Mech Phys Solids 1975;23:129.
[16] Stoneham AM. J Phys F 1971;1:778.
[17] Woo CH, Frank W. J Nucl Mater 1985;137:7.
[18] Krishan K. Radiat Eff 1982;66:121.
[19] Dubinko VI, Slezov VV, Tur AV, Yanovski VV. Radiat Eff 1986;100:85.
[20] Dubinko VI, Turkin AA. Appl Phys A 1994;58:21.
[21] Ghoiem NM, Walgraef D, Zinkle SJ. J Comp Aided Mater Design 2002;8:1.
[22] Walgraef D, Ghoiem NM. Phys Rev B 2003;67:064103.
[23] Imada M. J Phys Soc Jap 1978;45:1443.
[24] Kachaturyan AG. Theory of structural transformation in solids. Wiley; 1982.
[25] Suo Z, Lu W. J Nanopart Res 2000;2:333.
[26] Lu W, Suo Z. Phys Rev B 2002;65:085401.
[27] Lu W, Suo Z. J Mech Phys Solids 2001;49:1937.
[28] Hu SY, Chen LQ. Acta Mater 2001;49:463.
[29] Cahn JW, Hilliard JE. J Chem Phys 1958;28:258.
[30] Zhu Z, Chen LQ, Shen J, Tikare V. Phys Rev E 1999;60:3564.